Eigenvalue Optimization of the Energy-Balancing Feedback for Modular Multilevel Converters

Hendrik Fehr and Albrecht Gensior

***Abstract*—Despite its potential impact on the balancing performance, current literature on the modular multilevel converter (MMC) energy-balancing feedback gain design and tuning process seem incomplete. In order to close this research gap, the energy-balancing feedback gain tuning of an ac current controlled MMC with half-bridge cells and isolated star point is considered in this paper. The tuning is difficult, because each energy error adds its own dedicated component to the circulating current reference that leads to a strong coupling that evades common tuning approaches. This problem is solved in two steps: at first, the relevant error dynamics is extracted and validated to model the time domain behavior of the energy balancing. Second, a theorem from Wu (1975) is invoked to easily calculate the closed-loop eigenvalues that finally allow for an easy optimization of the energy-balancing performance. Despite the radical simplifications during the modeling and error dynamics extraction, the acquired model is able to adequately reproduce the energy errors and the balancing circulating current of the converter. Simulation and measurement results on a grid-side MMC demonstrate a considerable performance improvement in contrast to the traditional gain estimation on the open loop. This is verified with and without a second harmonic in the circulating currents.**

***Index Terms*—Control systems, energy balancing, modular multilevel converter (MMC), modeling.**

I. INTRODUCTION

THE family of modular multilevel converters [1]–[5] owes its advantages, but also its challenges, to the use of series-connected half-bridge or full-bridge cells [6], [7] without external supply. The modular multilevel converter (MMC) is one of the earliest members of this family and uses two series connections of cells per converter phase [8]. Each is equipped with a so-called arm inductor to suppress circulating currents [9], [10] and to allow for an independent voltage injection. The series connection paves the way for redundant [11] fault tolerant [12] generation of multilevel voltages while the local energy storage advantageously confines the power device commutation to each individual cell, unlinking the commutation circuit design from the number of voltage levels. However, as in a single-phase

---

Manuscript received August 14, 2018; revised November 14, 2018 and January 9, 2019; accepted February 9, 2019. Date of publication February 21, 2019; date of current version August 29, 2019. This work was supported by Deutsche Forschungsgemeinschaft under Grants GE 2502/4-1 and GE 2502/4-2. Recommended for publication by Associate Editor M. Saeedifard. *(Corresponding author: Hendrik Fehr.)*

The authors are with the Professur Leistungselektronik, Elektrotechnisches Institut, Technische Universität Dresden, 01069 Dresden, Germany (e-mail:

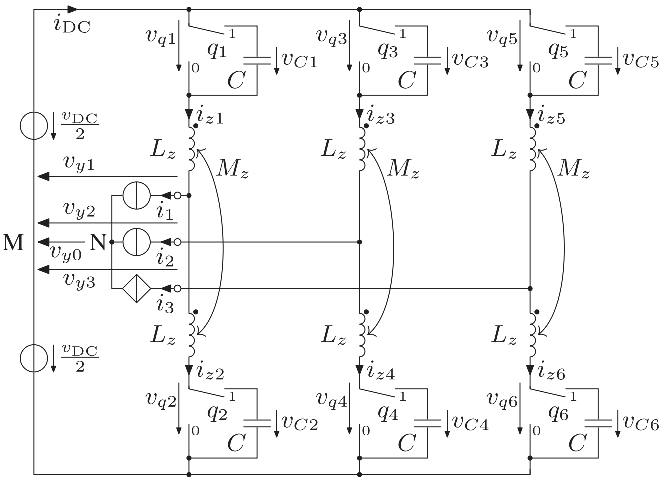

Fig. 1. Continuous model of an MMC using equivalent cells. The cells of each arm are represented by equivalent cells and their duty cycles $q_k \in [0, 1]$, $k = 1, \ldots, 6$ are used as control inputs. The load is given by current sources i_1, i_2, and the controlled current source $i_3 = -i_1 - i_2$ to ensure compliance with Kirchoff's first law at N. The load currents are assumed to be continuous and to match the initial currents of the inductors. See [55].

in contrast to the traditional gain estimation. This can be verified for the operation with suppressed circulating currents as well as when a second harmonic is used to reduce the voltage spread.

The paper is organized as follows. A model of the MMC arm energies and the parametrization of its variables are given in Section II in order to prepare the error dynamics extraction of the energy-balancing feedback. In Section III, the eigenvalues of the error dynamics are calculated in order to optimize their constellation in Section IV. Section V reports measurement results for a low-voltage MMC in order to compare the traditional gains with the optimized settings. Conclusions are given in Section VI.

II. MODELING

For the purpose of this paper, the cells of each arm are represented by an equivalent cell [53], [54], which simplifies an averaging process leading to a continuous model of an MMC as depicted in Fig. 1.

The corresponding mathematical modeling can be found in [55] and is briefly reflected in Section II-A. This prepares for the derivation of the error dynamics using a common energy feedback in Section II-B.

A. MMC Arm Energy Model

Modeling relies on the common summation and subtraction of upper and lower arm quantities in preparation of the Clarke transform

$$T_{0\alpha\beta} = \frac{1}{3}\begin{pmatrix} 1 & -1 & -1 \\ 2 & -1 & -1 \\ 0 & \sqrt{3} & -\sqrt{3} \end{pmatrix} = \begin{pmatrix} g_0 \\ g_\alpha \\ g_\beta \end{pmatrix} \tag{1}$$

whose second and last rows give rise to the complex rotation

$$\underline{g}_{dq} = \mathrm{e}^{-j\theta}\left(g_\alpha + jg_\beta\right) = \underline{a}_\theta^{-1}\left(g_\alpha + jg_\beta\right) \tag{2}$$

by the angle θ to facilitate notation in a rotating reference frame.

In a first step, the arm currents $i_{z1}, \ldots, i_{z6}$ and the output currents i_1, i_2, i_3 are transformed as

$$i_{s0} = g_0\left[(i_{z1}, i_{z3}, i_{z5})^{\mathrm{T}} + (i_{z2}, i_{z4}, i_{z6})^{\mathrm{T}}\right] \tag{3a}$$

$$0 = g_0(i_1, i_2, i_3)^{\mathrm{T}} \tag{3b}$$

$$\underline{i}_s = \underline{g}_{dq}\left[(i_{z1}, i_{z3}, i_{z5})^{\mathrm{T}} + (i_{z2}, i_{z4}, i_{z6})^{\mathrm{T}}\right] \tag{3c}$$

$$\underline{i} = \underline{g}_{dq}(i_1, i_2, i_3)^{\mathrm{T}} \tag{3d}$$

where $i_{s0} = \frac{2}{3}i_{\mathrm{DC}}$ is a scaled version of the dc current i_{DC} in Fig. 1, $\underline{i}_s$ denotes the circulating current, and $\underline{i}$ is the output current in complex notation. The zero sequence of the load currents (3b) is zero due to the isolated star point in Fig. 1.

Equivalently, the voltages are transformed as[1]

$$\begin{aligned} v_{x0} = g_0[&v_{\mathrm{DC}}(1,1,1)^{\mathrm{T}} - (v_{q1}, v_{q3}, v_{q5})^{\mathrm{T}} \\ &- (v_{q2}, v_{q4}, v_{q6})^{\mathrm{T}}] \end{aligned} \tag{4a}$$

$$v_{y0} = g_0(v_{y1}, v_{y2}, v_{y3})^{\mathrm{T}} \tag{4b}$$

$$\begin{aligned} \underline{v}_x = \underline{g}_{dq}[&v_{\mathrm{DC}}(1,1,1)^{\mathrm{T}} - (v_{q1}, v_{q3}, v_{q5})^{\mathrm{T}} \\ &- (v_{q2}, v_{q4}, v_{q6})^{\mathrm{T}}] \end{aligned} \tag{4c}$$

$$\begin{aligned} \underline{v}_y &= \underline{g}_{dq}(v_{y1}, v_{y2}, v_{y3})^{\mathrm{T}} \\ &= \underline{g}_{dq}\frac{1}{2}[(v_{q2}, v_{q4}, v_{q6})^{\mathrm{T}} - (v_{q1}, v_{q3}, v_{q5})^{\mathrm{T}} \\ &\quad - (L_z - M_z)\tfrac{\mathrm{d}}{\mathrm{d}t}(i_1, i_2, i_3)^{\mathrm{T}}] \end{aligned} \tag{4d}$$

where v_{y0} denotes the common-mode voltage and $\underline{v}_y$ the complex output voltage. The voltages v_{x0} and $\underline{v}_x$ drive the dc current and circulating current, respectively, which is reflected by their current dynamics

$$(L_z + M_z)\frac{\mathrm{d}}{\mathrm{d}t}\underline{i}_s = \underline{v}_x - j\omega(L_z + M_z)\underline{i}_s \tag{5a}$$

$$(L_z + M_z)\frac{\mathrm{d}}{\mathrm{d}t}i_{s0} = v_{x0} \tag{5b}$$

in which $\omega = \frac{\mathrm{d}}{\mathrm{d}t}\theta$ denotes the angular speed of the reference frame. By contrast, the output current $\underline{i}$ and its derivative $\frac{\mathrm{d}}{\mathrm{d}t}\underline{i}$ assume the role of time dependent parameters.

The self-inductance $L_z > 0$ and the mutual inductance $|M_z| \leq L_z$ are used to model the arm inductors and (if desired) their magnetic coupling. In a typical design, the mutual inductance M_z is positive to increase circulating current suppression in trade for a decreased inductance of the output current path. In high-voltage applications, one often refrains from using coupled inductors but in medium voltage applications this is a more common practice, e.g., [56]. See [57] for an analysis of various coupling opportunities for MMC arm inductors. This paper considers center-tapped arm inductors as in [58], [59]. The cases of uncoupled inductors and ideal coupling are covered as well by setting $M_z = 0$ or $|M_z| = L_z$, respectively.

---

[1] Factor $\frac{1}{2}$ is missing on the right-hand side of the second row of (4d) in [55].

In a second step, the arm energies are defined as

$$\begin{aligned} e_{zk} &= \frac{1}{2}Cv_{Ck}^2 + \frac{1}{2}(L_z + M_z)i_{zk}^2 - \frac{1}{4}M_z i_p^2 \\ p &= \left\lceil \frac{k}{2} \right\rceil, k = 1, \ldots, 6 \end{aligned} \tag{6}$$

in which v_{Ck} are the equivalent cell voltages and i_{zk} denotes the arm currents of the respective arm while i_p denotes the output current of the respective phase. The six arm energies $e_{z1}, \ldots, e_{z6}$ are transformed into two real variables and two complex variables

$$e_{s0} = 2g_0 \left[(e_{z1}, e_{z3}, e_{z5})^{\mathrm{T}} + (e_{z2}, e_{z4}, e_{z6})^{\mathrm{T}}\right] \tag{7a}$$

$$e_{d0} = 2g_0 \left[(e_{z1}, e_{z3}, e_{z5})^{\mathrm{T}} - (e_{z2}, e_{z4}, e_{z6})^{\mathrm{T}}\right] \tag{7b}$$

$$\underline{e}_s = 2\underline{g}_{dq} \left[(e_{z1}, e_{z3}, e_{z5})^{\mathrm{T}} + (e_{z2}, e_{z4}, e_{z6})^{\mathrm{T}}\right] \tag{7c}$$

$$\underline{e}_d = 2\underline{g}_{dq} \left[(e_{z1}, e_{z3}, e_{z5})^{\mathrm{T}} - (e_{z2}, e_{z4}, e_{z6})^{\mathrm{T}}\right]. \tag{7d}$$

Disregarding the scaling of $2/3$, the variables e_{s0} and e_{d0} denote the stored energy and the vertical energy difference between all upper and all lower arms, respectively. The complex energy sum $\underline{e}_s$ and energy difference $\underline{e}_d$ are given in dq-frame and together with the vertical difference e_{d0}, they represent the alternating part of the arm energies in stationary operation. In contrast to [55], the rotating frame is aligned to the voltage

$$\underline{v}_{y\Delta} = \underline{v}_y - M_z\left(j\omega\underline{i} + \tfrac{\mathrm{d}}{\mathrm{d}t}\underline{i}\right) \tag{8}$$

to ensure

$$\arg \underline{v}_{y\Delta} = 0 \tag{9}$$

and allows to represent $\underline{v}_{y\Delta}$ by means of its amplitude as

$$\underline{v}_{y\Delta} = \hat{v}_{y\Delta}. \tag{10}$$

This paves the way for a dynamic model of the MMC arm energies

$$\dot{e}_{s0} = v_{\mathrm{DC}} i_{s0} - \mathrm{Re}\big(\underline{i}\,\underline{v}_y^*\big) \tag{11a}$$

$$\dot{e}_{d0} = -2v_{y0} i_{s0} - \mathrm{Re}\big(\underline{i}_s^*\big)\,\hat{v}_{y\Delta} \tag{11b}$$

$$\dot{\underline{e}}_s = v_{\mathrm{DC}}\underline{i}_s - \underline{a}_\theta^{-3}\underline{v}_y^*\underline{i}^* - 2\underline{i}\,v_{y0} - j\omega\underline{e}_s \tag{11c}$$

$$\dot{\underline{e}}_d = v_{\mathrm{DC}}\underline{i} - \underline{a}_\theta^{-3}\underline{i}_s^*\hat{v}_{y\Delta} - 2\underline{i}_s v_{y0} - 2i_{s0}\hat{v}_{y\Delta} - j\omega\underline{e}_d. \tag{11d}$$

The superscript asterisk $(\cdot)^*$ denotes the complex conjugate in (11) and in the following. The energy balance (11a) equates the rate of change of the stored energy e_{s0} with the power difference between the dc side and ac side, respectively. The dynamics of the vertical energy difference e_{d0} is given by (11b) and is affected by both, the power generated by the common-mode voltage v_{y0} together with the dc current i_{s0} and the power generated by the output voltage $\hat{v}_{y\Delta}$ with the circulating current $\underline{i}_s$. The complex energy sum $\underline{e}_s$ and the complex energy difference $\underline{e}_d$ describe the remaining energy distribution among the arms. During normal operation with high dc voltage, the complex sum $\underline{e}_s$ is dominated by the power that the circulating current $\underline{i}_s$ generates w.r.t. the dc voltage v_{DC} and the complex difference $\underline{e}_d$ is dominated by the power that the output current $\underline{i}$ generates w.r.t. the dc voltage v_{DC}.

Although the alignment (9) is assumed in the following analysis, the results can be transferred to other alignments and implementations. In the special case of zero mutual inductance, i.e. $M_z = 0$, the alignment refers to the output voltage $\underline{v}_y$. In order to yield an unambiguous representation, the usual continuity assumptions apply to the voltage $\underline{v}_{y\Delta}$. Isolated discontinuities, as introduced by $\frac{\mathrm{d}}{\mathrm{d}t}\underline{i}$ at a reference step change of the current controller, correspond to a reinitialization of the system, i.e. they translate to an initial value problem in the analysis.

In conclusion, the current subsystem (5) and the energy subsystem (11) constitute a continuous model of an MMC. Rather than on equivalent cell voltages, the MMC model (11) relies on arm energies and favorably restricts the occurrence of the driving voltages v_{x0} and $\underline{v}_x$ to the corresponding current dynamics (5). This eliminates the need for approximating the capacitor voltage dynamics during the modeling, established e.g., in [60]. If desired, the equivalent cell voltages can be obtained from the arm energy definition (6) once the inverse of the transformation (7) is applied to the energy variables. However, cell voltage measurements are readily available in a typical implementation, rendering this calculation unnecessary.

The duty-cycles q_k of the equivalent cells are given by the fraction

$$q_k = \frac{v_{qk}}{v_{Ck}}, \quad k = 1, \ldots, 6 \tag{12}$$

in which the equivalent cell output voltage v_{qk} is obtained from the inverse of (4). The continuous model derived here is applicable to both types of cells: for half-bridge cells, the duty-cycles (12) are restricted to $q_k \in [0, 1]$ while full-bridge cells allow $q_k \in [-1, 1]$, $k = 1, \ldots, 6$.

B. Extracting the Error Dynamics

Assuming a lossless system, the total stored energy in the MMC is independent of the distribution among the arms, which motivates to neglect the stored energy and to focus solely on the energy distribution. This is achieved by discarding the subsystem (11a), as elaborated in the following.

In a typical setup, the dc current is dedicated to guide the total energy e_{s0} along its desired trajectory $t \mapsto e_{s0,\mathrm{d}}(t)$ leading to the reference

$$i_{s0,\mathrm{ref}} = \frac{\dot{e}_{s0,\mathrm{d}} + k_{es0}(e_{s0,\mathrm{d}} - e_{s0}) + \mathrm{Re}\big(\underline{i}\,\underline{v}_y^*\big)}{v_{\mathrm{DC}}} \tag{13}$$

for its scaled counterpart i_{s0} which is realized by a dc current controller

$$v_{x0} = (L_z + M_z)\frac{\mathrm{d}}{\mathrm{d}t}i_{s0,\mathrm{ref}} + k_{is0}(i_{s0,\mathrm{ref}} - i_{s0}) \tag{14}$$

resulting in the error dynamics

$$0 = \ddot{e}_{s0,\mathrm{err}} + k_1\dot{e}_{s0,\mathrm{err}} + k_0 e_{s0,\mathrm{err}} \tag{15}$$

of the energy error

$$e_{s0,\mathrm{err}} = e_{s0,\mathrm{d}} - e_{s0}. \tag{16}$$

The error dynamics (15) is found by successively eliminating from the derivative of the subsystem (11a), in order, $\frac{\mathrm{d}}{\mathrm{d}t}i_{s0}$,

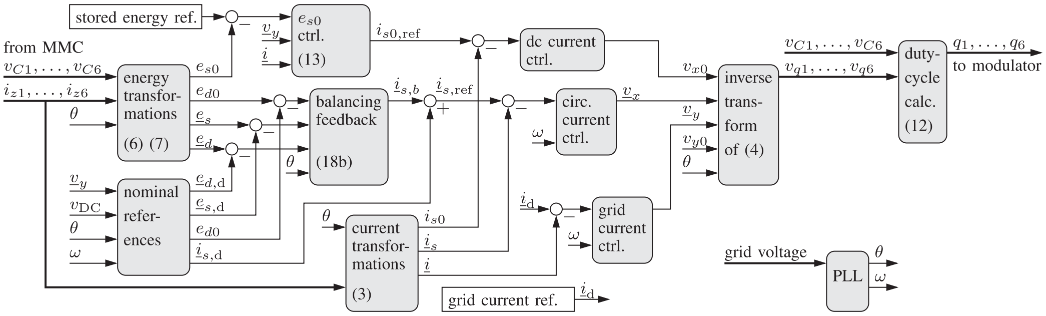

Fig. 2. Block diagram of the MMC control scheme, including the balancing controller based on the circulating current reference (18).

v_{x0}, $i_{s0,\text{ref}}$, and i_{s0} with the help of subsystem (5b), controller (14), reference (13), and subsystem (11a), respectively. Now the error (16) and its derivatives as well as the coefficients $k_1 = k_{es0} + k_0/k_{es0}$ and $k_0 = k_{es0}k_{is0}/(L_z + M_z)$ can be identified, yielding (15). Due to the output power compensation in the current reference (13), excitation of the error dynamics (15) is mainly caused by measurement and implementation inaccuracies implying only small energy errors. Moreover, the other energies will not disturb the total energy controller, because the corresponding subsystem is independent of the circulating current $\underline{i}_s$, supporting the separation.

This separation of the subsystem (11a) means that the stored energy e_{s0} can be controlled independently of the other energies and thus, the corresponding error $e_{s0,\text{err}}$ is assumed to be small, compared to the energy errors

$$e_{d0,\text{err}} = e_{d0} - e_{d0,\text{d}} \tag{17a}$$

$$\underline{e}_{s,\text{err}} = \underline{e}_s - \underline{e}_{s,\text{d}} \tag{17b}$$

$$\underline{e}_{d,\text{err}} = \underline{e}_d - \underline{e}_{d,\text{d}}. \tag{17c}$$

The energies e_{d0}, $\underline{e}_s$, and $\underline{e}_d$ constitute the energy distribution and usually, their nominal values $e_{d0,\text{d}}$, $\underline{e}_{s,\text{d}}$, and $\underline{e}_{d,\text{d}}$ describe a balanced operation. Thus, energy balancing can be regarded as reducing the errors (17) and is commonly achieved by positive and negative sequence circulating currents as well as a dc component of the circulating current. In a nutshell, the circulating current reference becomes

$$\underline{i}_{s,\text{ref}} = \underline{i}_{s,\text{d}} + \underline{i}_{s,b} \tag{18a}$$

$$\underline{i}_{s,b} = \underbrace{k_s\,\underline{e}_{s,\text{err}}}_{\text{horizontal}} - \underbrace{k_d\underline{e}^*_{d,\text{err}}\underline{a}_\theta^{-3}}_{\text{vertical (neg. seq.)}} - \underbrace{k_0\,e_{d0,\text{err}}}_{\text{vertical (pos. seq.)}} \tag{18b}$$

in which $\underline{i}_{s,\text{d}}$ is the nominal circulating current and $\underline{i}_{s,b}$ is the balancing feedback while k_s, k_d, and k_0 denote constant proportional gains. In contrast to the *standard balancing* in [55], the alignment (9) already maximizes the balancing effect, rendering additional rotations unnecessary. Except for the use of a different reference frame, the balancing feedback (18b) equals the *hf-mode* in [32] and provides very good balancing. A block diagram of the control scheme based on this balancing feedback is shown in Fig. 2.

TABLE I
PARAMETERS OF THE MMC FOR SIMULATIONS AND EXPERIMENTS

parameter	symbol	value
dc voltage	v_{DC}	580 V
output voltage	$\lvert\underline{v}_y\rvert$	285 V
angular frequency	ω	2π 50 Hz
number of cells per arm	n	6
cell capacitance	C_{SM}	0.375 mF
arm inductance	L_z	1.2 mH
mutual inductance	M_z	0.94 mH
sampling time	T	205 µs
load inductance		15 mH
stored energy	e_{s0}	48.05 J
rotating frame alignment voltage (10)	$\hat{v}_{y\Delta}$	284.14 V
grid current reference	$\underline{I}$	7.5 A∠−157°
grid frequency	ω	2π50 Hz
angle at load step	θ_0	89.6°

The error dynamics will be established w.r.t. a nominal solution of the subsystems (11b), (11c), and (11d), namely

$$\dot{e}_{d0,\text{d}} = -2v_{y0}i_{s0} - \text{Re}\big(\underline{i}^*_{s,\text{d}}\big)\,\hat{v}_{y\Delta} \tag{19a}$$

$$\underline{\dot{e}}_{s,\text{d}} = v_{\text{DC}}\underline{i}_{s,\text{d}} - \underline{a}_\theta^{-3}\underline{v}_y^*\underline{i}^* - 2\underline{i}\,v_{y0} - j\omega\underline{e}_{s,\text{d}} \tag{19b}$$

$$\begin{aligned}\underline{\dot{e}}_{d,\text{d}} &= v_{\text{DC}}\underline{i} - \underline{a}_\theta^{-3}\underline{i}^*_{s,\text{d}}\hat{v}_{y\Delta} - 2\underline{i}_{s,\text{d}}v_{y0}\\ &\quad - 2i_{s0}\hat{v}_{y\Delta} - j\omega\underline{e}_{d,\text{d}}.\end{aligned} \tag{19c}$$

Inserting the circulating current (18a) into the subsystems (11b), (11c), and (11d) before subtracting the nominal solution (19), the error dynamics emerges as

$$\begin{aligned}\dot{e}_{d0,\text{err}} &= \hat{v}_{y\Delta}\text{Re}\big(k_s\underline{e}^*_{s,\text{err}} - k_d\underline{e}_{d,\text{err}}\underline{a}_\theta^3\big)\\ &\quad - e_{d0,\text{err}}k_0\hat{v}_{y\Delta}\end{aligned} \tag{20a}$$

$$\begin{aligned}\underline{\dot{e}}_{s,\text{err}} &= v_{\text{DC}}\left[e_{d0,\text{err}}k_0 - \underline{e}_{s,\text{err}}k_s + \underline{e}^*_{d,\text{err}}k_d\underline{a}_\theta^{-3}\right]\\ &\quad - j\omega\underline{e}_{s,\text{err}}\end{aligned} \tag{20b}$$

$$\begin{aligned}\underline{\dot{e}}_{d,\text{err}} &= \hat{v}_{y\Delta}\left[(\underline{e}^*_{s,\text{err}}k_s - e_{d0,\text{err}}k_0)\underline{a}_\theta^{-3} - \underline{e}_{d,\text{err}}k_d\right]\\ &\quad + 2v_{y0}\left[\underline{e}_{s,\text{err}}k_s - e_{d0,\text{err}}k_0 - \underline{e}^*_{d,\text{err}}k_d\underline{a}_\theta^{-3}\right]\\ &\quad - j\omega\underline{e}_{d,\text{err}}.\end{aligned} \tag{20c}$$

Replacing the circulating current with its reference (18a) and using the nominal solution (19) is equivalent to assuming an ideal current control, which is justified by the inherently slower dynamics of the energy imbalance compared to the current con-

TABLE II
OVERVIEW OF THE SIMULATION AND EXPERIMENTAL RESULTS FOR DIFFERENT GAIN SETTINGS

Description	Constellation	Gain Setting in A/J k_0	k_s	k_d	zero circulating current simulation	experiment	with 2nd harmonic simulation	experiment
zero gain	○ in Fig. 7a	0	0	0				
traditional setting (see Appendix)	× in Fig. 7b	0.18	0.42	0.18	Figs. 3, 4, 8, 9	Figs. 10, 12	Figs. 5, 6	Figs. 13, 15
optimized setting (see Section IV)	• in Fig. 7b	0.61	0.20	0.58	Figs. 8, 9	Figs. 11, 12		Figs. 14, 15

trollers. Moreover, the error dynamics (20) is valid for any circulating current injection of the nominal circulating current $\underline{i}_{s,\mathrm{d}}$, provided the nominal circulating current and the energy references satisfy (19). This includes a second harmonic circulating current for reduced capacitor voltage ripple as in [61], [62], or a loss minimizing waveform as in [63].

The error dynamics is validated against the simulation of a switched model of a complete MMC including current controllers, phase locked loop (PLL), sampling delays, and modulation down to the individual cells which is referred to as *extensive model*. The simulation parameters for the validation are given in Table I.

To begin with, the gain settings for the balancing control (18b) are estimated individually from a simplified model for each energy, according to [32], [48]. This simplified gain determination on the open loop is denoted traditional setting in the course of this paper and is discussed in more detail in the appendix. The validation uses the traditional settings as given in the second row of Table II. Fig. 3 shows the results for the extensive model during a step change of the output current from zero to $\underline{I}$. The cell voltages of the switched model experience the usual imbalance induced by the sudden output current change as visible in Fig. 3(a). Balancing takes a few periods and requires only a small additional circulating current, as visible by comparing the arm currents in Fig. 3(c) with the output currents in Fig. 3(e). However, a considerable portion of the control reserve is taken up by the compensation of the cell voltage deviations as visible from the duty-cycles in Fig. 3(b). This general behavior can be observed for other step changes as well as for a step change back to zero.

In Fig. 4, the error dynamics (20) is compared against the extensive model by solving the initial value problem for the same step change and recovering the energies with (17), i.e. by adding the nominal solution to the solution of (20). Blue and red traces in Fig. 4 indicate results of the error dynamics (20) while gray traces correspond to the respective variables of the extensive model and are taken from the simulation results in Fig. 3. The good performance of the output current controller, visible in Fig. 4(a), supports the assumption of ideal output current control. The stance of discarding the total stored energy e_{s0} during the extraction of the error dynamics (20) is supported by the negligible deviations shown in Fig. 4(b). Of course, the simplified model is not able to capture the full dynamic response because some information is lost for the sake of simplifying the problem. Apart from the neglected current control dynamics, the differences between the extensive model and the simplified error dynamics originate primarily from modulation effects (e.g., voltage errors [64], [65], cell voltage imbalances, and quantization errors [66]) and the time-discrete control implementation which are not reproduced by the equivalent cells of the continuous model. Deviations are most obvious in Fig. 4(f) where the balancing circulating current of both models agrees sufficiently during the first few fundamental periods after the step change when the energy imbalance dominates the system behavior. When the energy errors decay, the resemblance worsens,

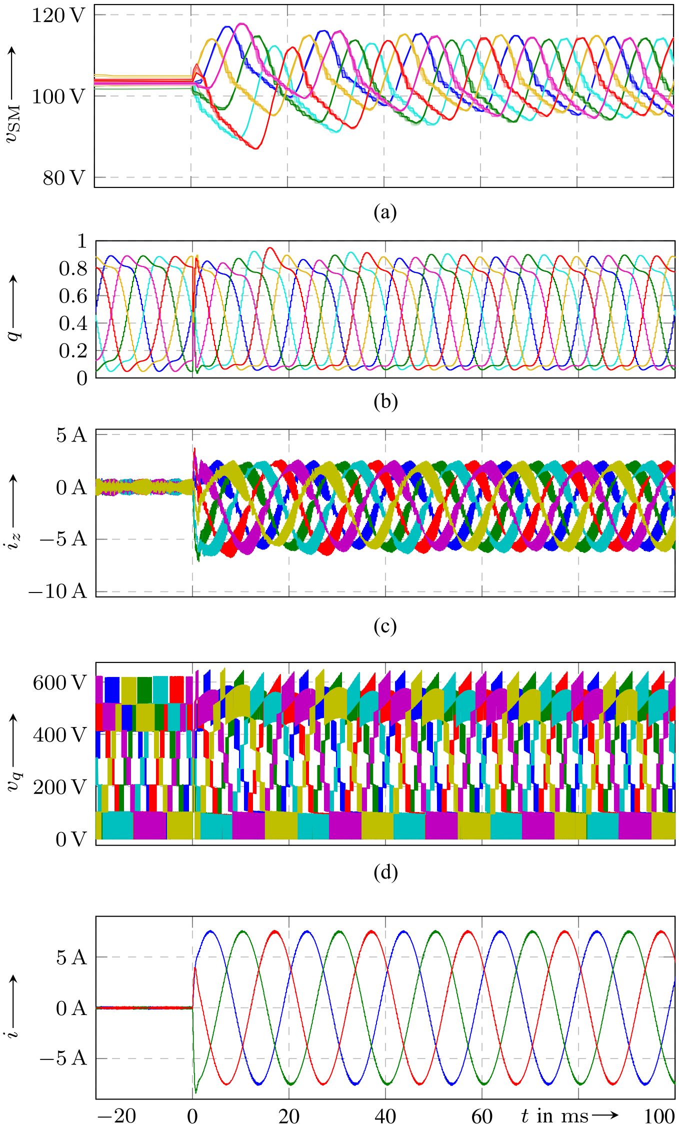

(a)

(b)

(c)

(d)

(e)

Fig. 3. Simulation results when the nominal circulating current is zero: (a) cell voltages, (b) duty-cycles, (c) arm currents, (d) injected arm voltages, (e) output currents. During an output current reference step change at $t = 0$ from zero to $\underline{I}$.

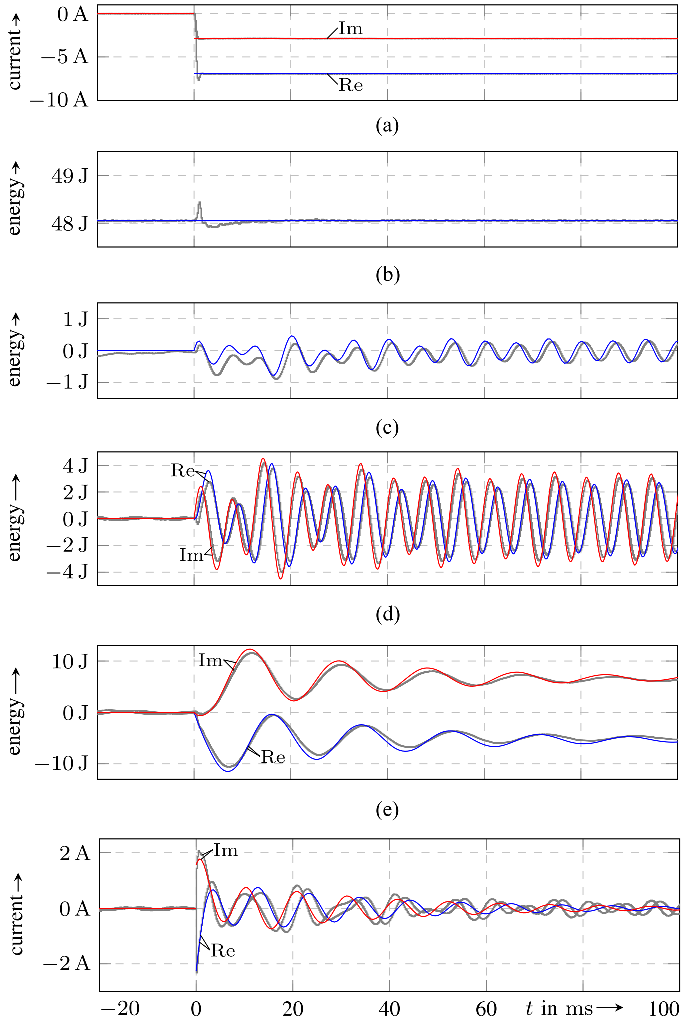

(f)

Fig. 4. Validation of the error dynamics (20) (blue and red solid lines) against the simulation of the extensive model (gray staircase lines), during an output current reference step change at $t = 0$ from zero to $\underline{I}$ when the nominal circulating current $\underline{i}_{s,\mathrm{d}}$ is zero: (a) Output current in rotating frame; (b) Stored energy e_{s0}; (c) Vertical difference e_{d0}; (d) Complex sum $\underline{e}_s$; (e) Complex difference $\underline{e}_d$; (f) Balancing circulating current $\underline{i}_{s,b}$ according to (18b). The error dynamics (20) is reinitialized at $t = 0$ to account for the step change.

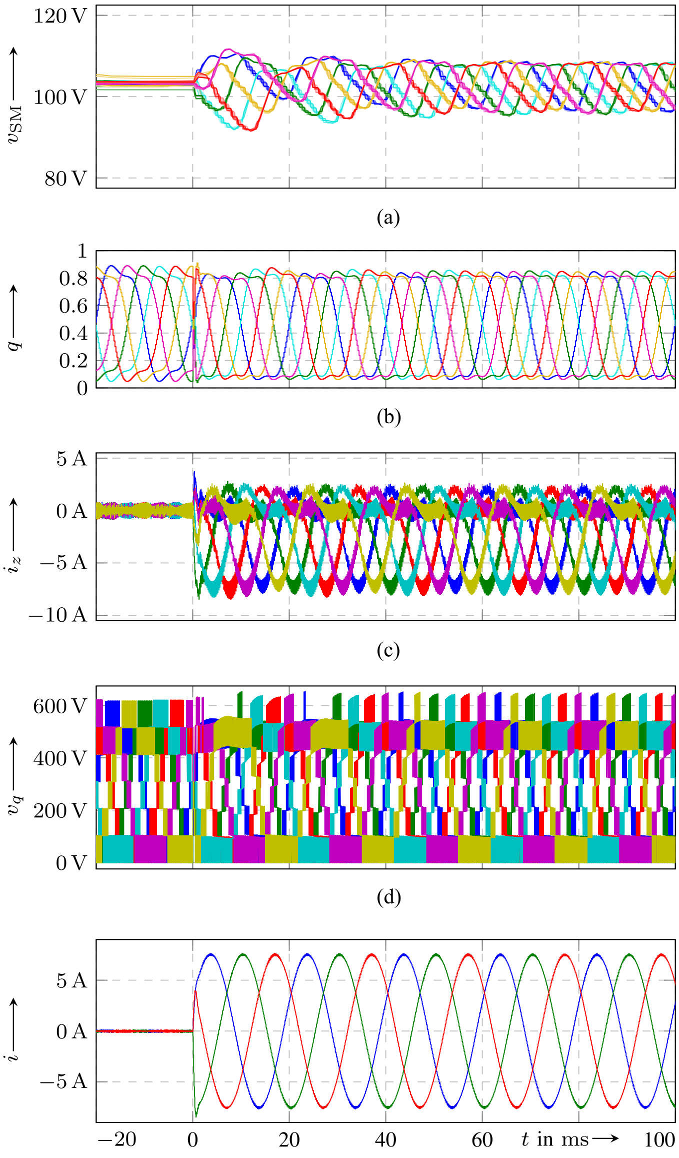

(e)

Fig. 5. Simulation results for a second harmonic in the nominal circulating current: (a) cell voltages, (b) duty-cycles, (c) arm currents, (d) injected arm voltages, (e) output currents. During an output current reference step change at $t = 0$ from zero to $\underline{I}$.

because the neglected effects start to dominate in the extensive model.

In Figs. 5 and 6, the extracted error dynamics is validated for the case when a second harmonic is used for the nominal circulating current to reduce the capacitor voltage ripple.

Here too, the solution of the simplified error dynamics (20) acceptably resembles the energies and the balancing circulating current component $\underline{i}_{s,b}$ of the extensive MMC simulation, even though the second harmonic circulating current reference causes higher current control errors. In comparison to Fig. 4, the differences between both models in Fig. 6 appear larger in relation to the nominal regime because the step change induces a smaller energy imbalance due to the reduced voltage ripple operation.

Despite the radical simplifications during the modeling and error dynamics extraction, the acquired system (20) is able to suitably approximate the energies and the balancing circulating current of the extensive model, given just an initial value, justifying the simplifications made. The good agreement of the simplified error dynamics (20) with the results of an extensive simulation during the first fundamental periods after the step change confirms its usefulness for the feedback gain tuning. The following analysis proceeds with the error dynamics in order to improve the settings of the proportional gains k_0, k_s, and k_d.

III. EIGENVALUE CALCULATION

A. *Recall of the Main Result in [52]*

The theorem in [52] states that the state transition matrix of a linear, time-varying (autonomous) system

$$\dot{x}(t) = \boldsymbol{A}(t)x(t), \quad x \in \mathbb{R}^{\nu}, \quad t \mapsto \boldsymbol{A}(t) \ni \mathbb{R}^{\nu\times\nu} \tag{21}$$

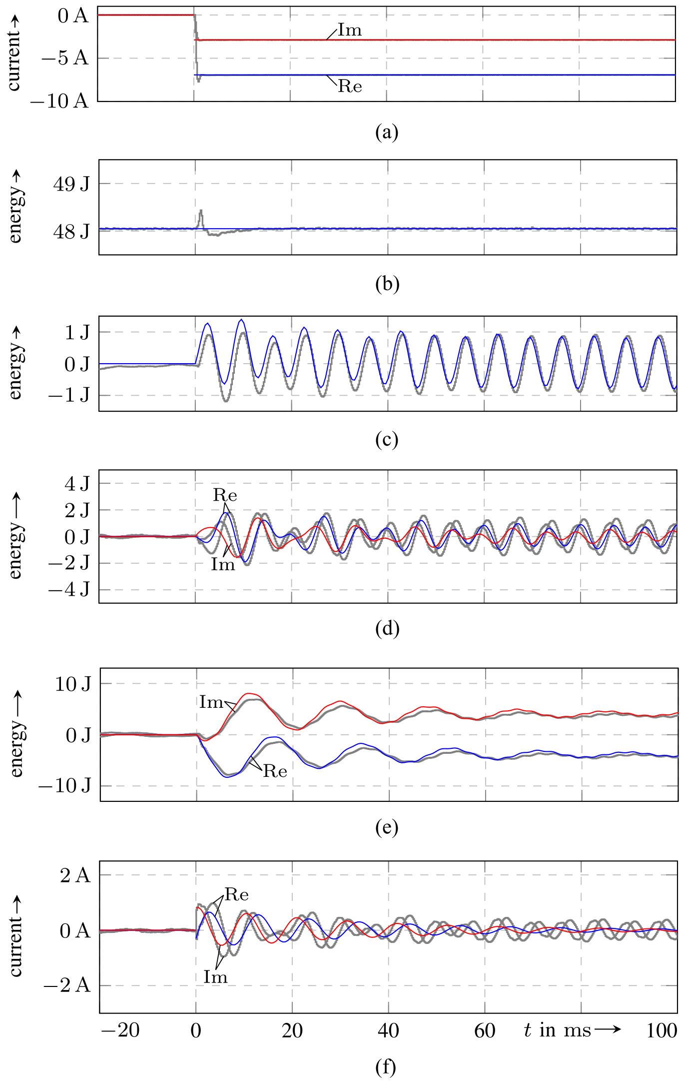

(a)

(b)

(c)

(d)

(e)

(f)

Fig. 6. Validation of the error dynamics (20) (blue and red solid lines) against the simulation of the extensive model (gray staircase lines), during an output current reference step change at $t = 0$ from zero to $\underline{I}$ when a second harmonic is used in the circulating current: (a) Output current in rotating frame; (b) Stored energy e_{s0}; (c) Vertical difference e_{d0}; (d) Complex sum $\underline{e}_s$; (e) Complex difference $\underline{e}_d$; (f) Balancing circulating current $\underline{i}_{s,b}$ according to (18b). The error dynamics (20) is reinitialized at $t = 0$ to account for the step change.

of order $\nu \in \mathbb{N}^+$ is given by

$$\boldsymbol{\Phi}(t,0) = \mathrm{e}^{\boldsymbol{A}_1 t}\mathrm{e}^{\boldsymbol{A}_2 t} \tag{22}$$

if and only if there exists a constant matrix $\boldsymbol{A}_1$, which satisfies the relation

$$\boldsymbol{A}_1\boldsymbol{A}(t) - \boldsymbol{A}(t)\boldsymbol{A}_1 = \dot{\boldsymbol{A}}(t). \tag{23}$$

The second constant matrix $\boldsymbol{A}_2$ in (22) is then given by

$$\boldsymbol{A}_2 = \boldsymbol{A}(0) - \boldsymbol{A}_1. \tag{24}$$

Following [52] further, the transformation

$$x = \mathrm{e}^{\boldsymbol{A}_1 t}\bar{x} \tag{25}$$

brings (21) into the linear time-invariant system

$$\dot{\bar{x}} = \boldsymbol{A}_2\bar{x}. \tag{26}$$

Finally, the results in [52] include a stability criterion of (21), involving the joined eigenvalues of $\boldsymbol{A}_1$ and $\boldsymbol{A}_2$ as follows: let $\underline{\lambda}_{1,l}$ be the lth eigenvalue of $\boldsymbol{A}_1$ and $\underline{\lambda}_{2,k}$ be the kth eigenvalue of $\boldsymbol{A}_2$, then asymptotic stability of (21) is assured if

$$\mathrm{Re}\big(\underline{\lambda}_{1,l}\big) + \mathrm{Re}\big(\underline{\lambda}_{2,k}\big) < 0 \quad \forall l,k \in 1,\ldots,\nu. \tag{27}$$

Direct application of this theorem requires that the eigenvalues of $\boldsymbol{A}(t)$ are independent of t [52].

B. Application of the Method to the Error Dynamics (20)

By means of the state definition

$$\begin{aligned}\mathbb{R}^5 \ni x = \big[&e_{d0}, \mathrm{Re}\big(\underline{e}_{s,\mathrm{err}}\big), \mathrm{Im}\big(\underline{e}_{s,\mathrm{err}}\big)\\ &\mathrm{Re}\big(\underline{e}_{d,\mathrm{err}}\big), \mathrm{Im}\big(\underline{e}_{d,\mathrm{err}}\big)\big]^{\mathrm{T}}\end{aligned} \tag{28}$$

the error dynamics (20) presents itself in the form (21). In the case of zero common-mode voltage, i.e. $v_{y0} = 0$, the system matrix $\boldsymbol{A}$ is given by

$$\boldsymbol{A} = \boldsymbol{A}_k + \cos(3\theta)\boldsymbol{A}_d + \sin(3\theta)\boldsymbol{A}_q \tag{29}$$

in which the matrices $\boldsymbol{A}_k$, $\boldsymbol{A}_d$, and $\boldsymbol{A}_q$ are written with the help of the abbreviations

$$a = k_0\hat{u}_{y\Delta} \quad b = k_s v_{\mathrm{DC}} \quad c = k_d\hat{v}_{y\Delta} \tag{30a}$$

$$d = k_0 v_{\mathrm{DC}} \quad e = k_s\hat{v}_{y\Delta} \quad f = k_d v_{\mathrm{DC}} \tag{30b}$$

as[2]

$$\boldsymbol{A}_k = \begin{pmatrix} -a & e & 0 & 0 & 0\\ d & -b & \omega & & \\ 0 & -\omega & -b & & \\ 0 & & & -c & \omega\\ 0 & & & -\omega & -c \end{pmatrix} \tag{31}$$

$$\boldsymbol{A}_d = \begin{pmatrix} 0 & 0 & 0 & -c & 0\\ 0 & & & f & \\ 0 & & & & -f\\ -a & e & & & \\ 0 & & -e & & \end{pmatrix} \tag{32}$$

$$\boldsymbol{A}_q = \begin{pmatrix} 0 & 0 & 0 & 0 & c\\ 0 & & & & -f\\ 0 & & & -f & \\ 0 & & -e & & \\ a & -e & & & \end{pmatrix}. \tag{33}$$

Since v_{DC} and $\hat{v}_{y\Delta}$ are assumed to be constant, the only time dependence of the system matrix $\boldsymbol{A} \in \mathbb{R}^{5\times 5}$ is caused by the angle θ. Especially in medium-voltage applications this assumption is permissible because the time horizon in which load transfers take place—and $\hat{v}_{y\Delta}$ is not constant—is much shorter than the time needed to reestablish a balanced operating regime w.r.t. the energies.

---

[2] Zero entries are omitted except in the first row and column, respectively.

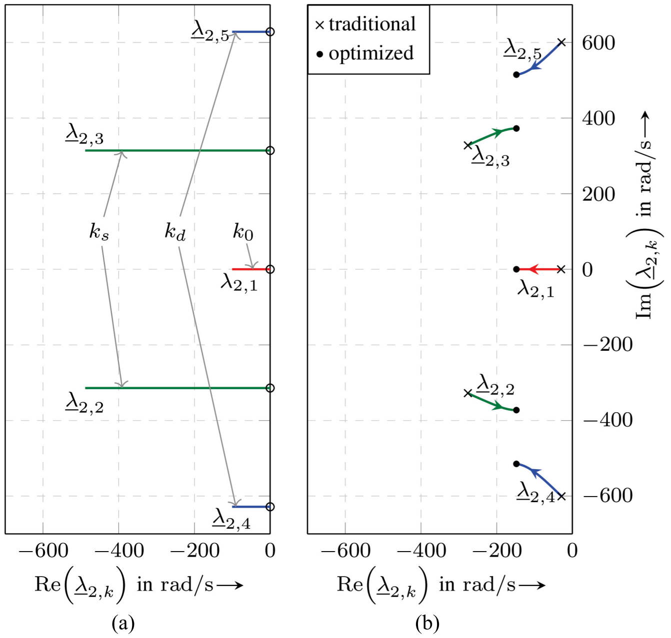

Fig. 7. Eigenvalues of $\boldsymbol{A}_2$ during (a) separate variation and (b) simultaneous variation of the gains k_0, k_s, and k_d. The separate variation decreases the real part of the eigenvalues and demonstrates the expected correspondence of each gain to one eigenvalue or one eigenvalue pair. The other eigenvalues remain on the imaginary axis as indicated by the circles ○. This mapping is lost when more than one gain is nonzero, as with the constellations in (b) on the right. All gains are changed simultaneously from the traditional to the optimized setting (see Table II), indicating a damping improvement of the optimized constellation.

Despite of the fact that $\boldsymbol{A}$ changes periodically, its eigenvalues are constant because its characteristic polynomial is free of θ and[3]

$$\boldsymbol{A}_1 = \begin{pmatrix} \boldsymbol{E}_3 & \\ & \begin{bmatrix} & 3\omega \\ -3\omega & \end{bmatrix} \end{pmatrix} \tag{34}$$

is a solution of (23). The matrix exponential of $\boldsymbol{A}_1 t$ is

$$\mathrm{e}^{\boldsymbol{A}_1 t} = \begin{pmatrix} \boldsymbol{E}_3 & \\ & \begin{bmatrix} \cos(3\omega t) & \sin(3\omega t) \\ -\sin(3\omega t) & \cos(3\omega t) \end{bmatrix} \end{pmatrix} \tag{35}$$

which is found by diagonalization

$$\boldsymbol{A}_1 = \boldsymbol{S}\,\mathrm{diag}(0, 0, 0, -j3\omega, j3\omega)\,\boldsymbol{S}^{-1} \tag{36}$$

with the help of matrix

$$\boldsymbol{S} = \begin{pmatrix} \boldsymbol{E}_3 & \\ & \begin{bmatrix} 1 & 1 \\ -j & j \end{bmatrix} \end{pmatrix}. \tag{37}$$

The corresponding matrix $\boldsymbol{A}_2$ reads

$$\boldsymbol{A}_2 = \boldsymbol{A}_k + \cos(3\theta_0)\boldsymbol{A}_d + \sin(3\theta_0)\boldsymbol{A}_q - \boldsymbol{A}_1 \tag{38}$$

in which θ_0 denotes the angle θ at the instant $t = 0$. The eigenvalues of $\boldsymbol{A}_2$ are independent of θ_0.

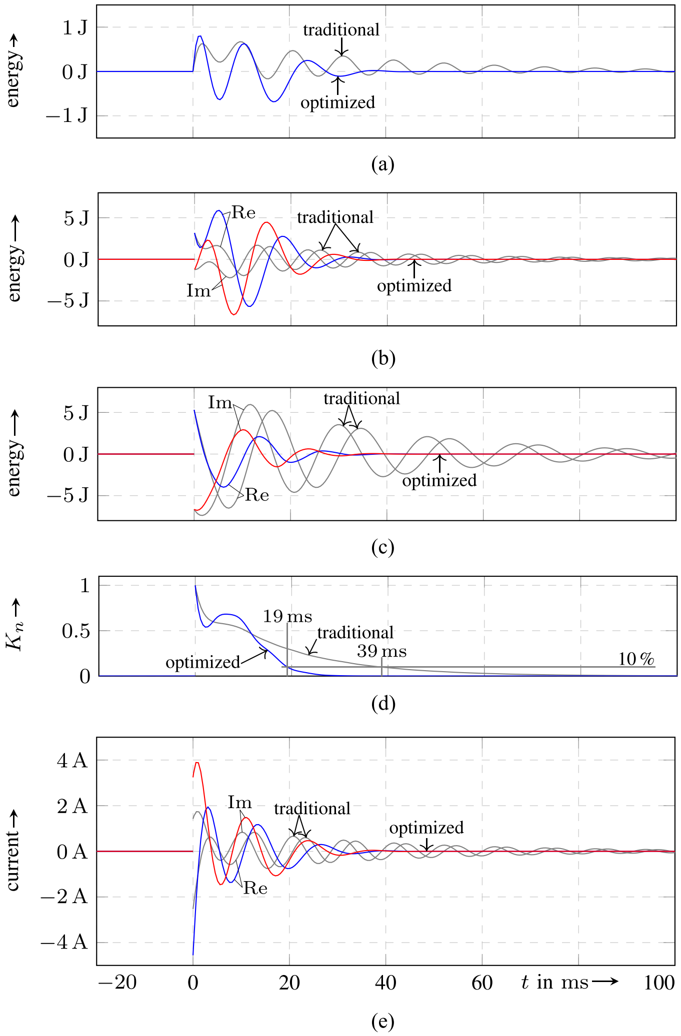

(a)

(b)

(c)

(d)

(e)

Fig. 8. Comparison of the optimized settings (blue and red) with the traditional gains from Table II (gray) via simulation of the error dynamics (20): (a) Error $e_{d0,\mathrm{err}}$ of the vertical difference; (b) Error $\underline{e}_{s,\mathrm{err}}$ of the complex sum; (c) Error $\underline{e}_{d,\mathrm{err}}$ of the complex difference; (d) Normalized sum of the squared errors (43); (e) Balancing circulating current $\underline{i}_{s,b}$ according to (18b). The output current is the same as in Fig. 4(a), while the initial values of (20) belong to an operation regime with zero common-mode voltage.

The eigenvalues of $\boldsymbol{A}_1$ are given by

$$\begin{aligned} \underline{\lambda}_{1,1} &= \underline{\lambda}_{1,2} = \underline{\lambda}_{1,3} = 0 \\ \underline{\lambda}_{1,4} &= \underline{\lambda}_{1,5}^* = -j3\omega \end{aligned} \tag{39}$$

and do not contribute any damping as their real parts are zero. Consequently, the eigenvalues of $\boldsymbol{A}_2$ need to lie left of the imaginary axis. In preparation for the optimization, the eigenvalues of $\boldsymbol{A}_2$ are visualized in Fig. 7 in the complex plane. Fig. 7(a) depicts the eigenvalue loci of $\boldsymbol{A}_2$ when each gain k_0, k_s, and k_d is individually increased from zero to the value of the traditional setting in Table II while the other two gains are kept at zero. The separate variation demonstrates a simple correspondence between increased damping of individual eigenvalues and one of the gains k_0, k_s, and k_d, as expected from the damping terms in each subsystem of the error dynamics (20).

The constellation in Fig. 7(b) indicated by cross-marks × corresponds to the traditional settings from Table II and reflects

---

[3] $\boldsymbol{E}_m$ denotes the $m \times m$ identity matrix.

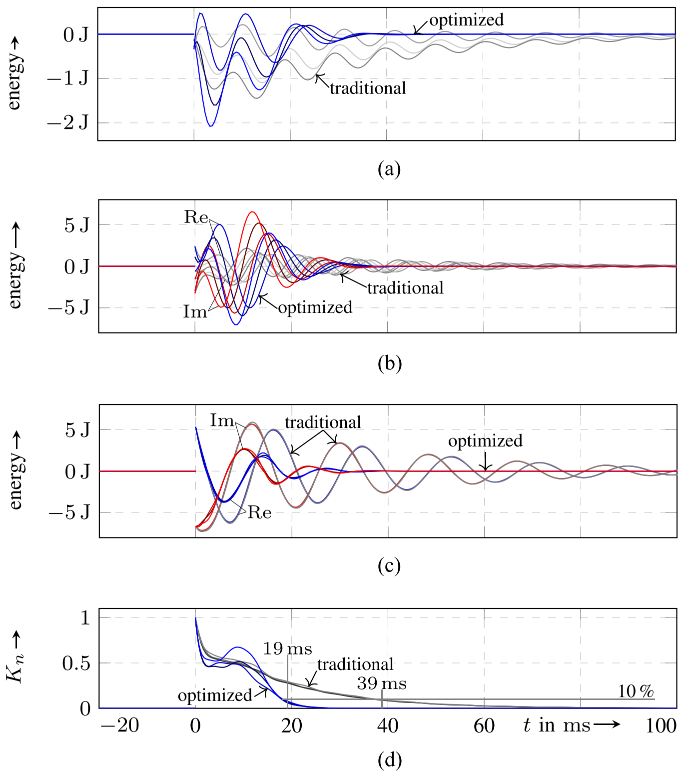

Fig. 9. Family of solutions obtained from the error dynamics (20) during variation of the initial angle θ_0, in order to compare the traditional gains with the optimized settings in case of *triplen harmonic injection* (see Table II): (a) Error $e_{d0,\mathrm{err}}$ of the vertical difference; (b) Error $\underline{e}_{s,\mathrm{err}}$ of the complex sum; (c) Error $\underline{e}_{d,\mathrm{err}}$ of the complex difference; (d) Normalized sum of the squared errors (43). The output current changes at $t = 0$ from zero to $\underline{I}$. The 10% line is the same as in Fig. 8(d) to facilitate comparison. The superior performance of the optimized gains is retained even for the case with nonzero common-mode voltage.

a high damping for the complex conjugate pair $\underline{\lambda}_{2,2}$, $\underline{\lambda}_{2,3}$ and a low damping for the complex conjugate pair $\underline{\lambda}_{2,4}$, $\underline{\lambda}_{2,5}$. The high damping originates from the separate treatment of each energy by ignoring the mutual coupling, which allows an all too optimistic assumption of a fast behavior of the energy $\underline{e}_s$. This leads to a high gain but endangers a practical damping compromise w.r.t. the other energies, as visible from the smaller distance to the imaginary axis of the eigenvalues $\lambda_{2,1}$, $\underline{\lambda}_{2,4}$, and $\underline{\lambda}_{2,5}$.

IV. OPTIMIZATION

The three gains of the feedback circulating current (18b) are insufficient for an eigenvalue placement of $\boldsymbol{A}_2$, suggesting the use of a cost function to optimize the eigenvalue constellation. Placing both complex conjugate eigenvalue pairs in the region of the bisecting lines $\mathrm{Re}(\underline{\lambda}) = \pm\mathrm{Im}(\underline{\lambda})$ with the constellations in [67, p. 88] in mind was not possible. However, tuning all eigenvalues to have the same real part was possible by minimizing the cost function

$$\begin{aligned} K_{\mathrm{Re}(\underline{\lambda})} = {} & \max(L_{\mathrm{Re}(\underline{\lambda})}) - \min(L_{\mathrm{Re}(\underline{\lambda})}) \\ & + 3\max(L_{\mathrm{Re}(\underline{\lambda})}) \end{aligned} \qquad (40)$$

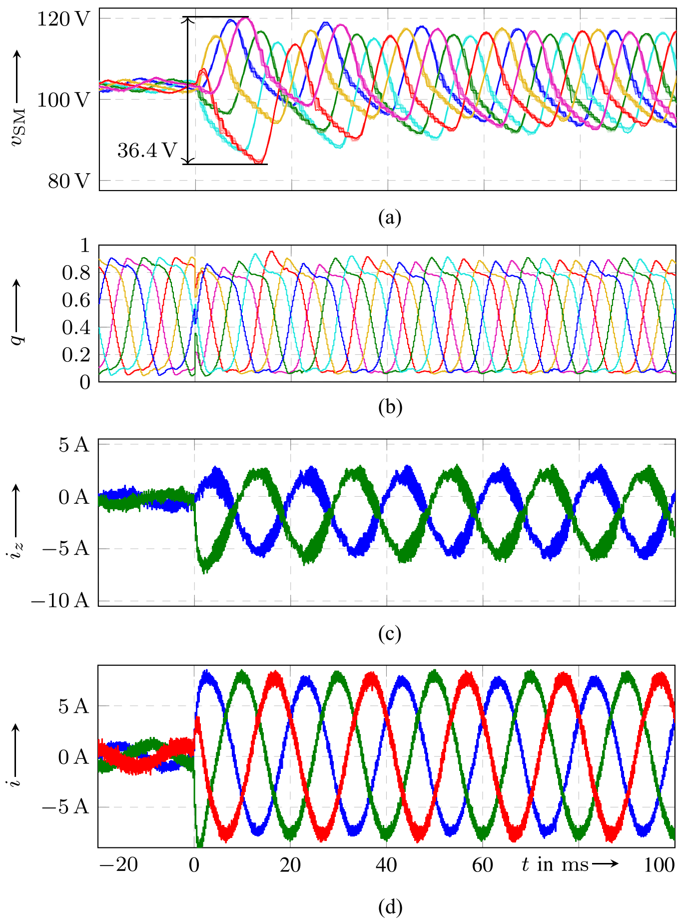

Fig. 10. Measurement results of the traditional gain settings (Table II): (a) cell voltages, (b) duty-cycles, (c) arm currents, and (d) output currents during an output current reference step change at $t = 0$. The energy errors of the same experiment are shown with blue and red traces in Fig. 12.

which operates on the list of real parts

$$L_{\mathrm{Re}(\underline{\lambda})} = \left[\mathrm{Re}\left(\underline{\lambda}_{2,1}\right), \ldots, \mathrm{Re}\left(\underline{\lambda}_{2,5}\right)\right]. \qquad (41)$$

The cost function (40) favors constellations with smaller differences between the minimum and maximum real part such that all eigenvalues eventually have the same real part. In order to reward constellations that provide higher damping, a threefold penalty for the largest real part is included as well. Using Matlab's *fminsearch* to minimize the cost function (40) for the parameters in Table I results in the optimized gains in the bottom most row of Table II. The lines in Fig. 7(b) depict the eigenvalue loci when the gains are changed from the traditional setting to the optimized values. The eigenvalues in the latter case are indicated by solid dots • and enjoy nearly the same real part. The optimized gains k_0 and k_d for the vertical difference and the complex difference are higher in trade for a much lower gain k_s for the complex sum resulting in a superior constellation with good damping. The simplified estimation on the open loop will—even for different setups—unlikely deliver a comparable gain setting because of its systematic tendency to high values for k_s and, at the same time, low values for k_0 and k_d.

The simulation results of the error dynamics (20) in Fig. 8 demonstrate a much faster decay of the energy errors when the

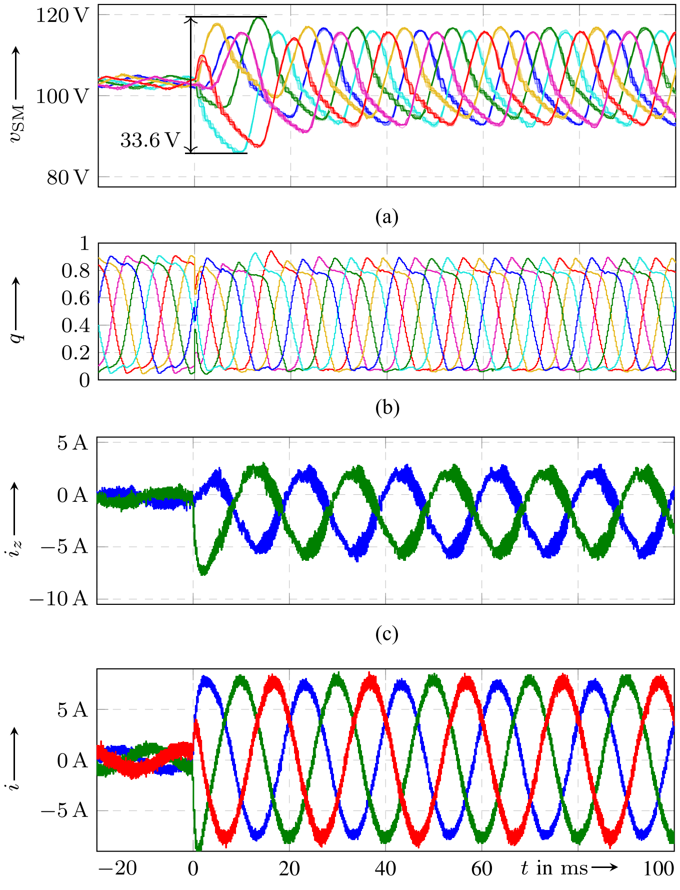

(a)

(b)

(c)

(d)

Fig. 11. Measurement results for the optimized gains from Table II: (a) cell voltages, (b) duty-cycles, (c) arm currents, and (d) output currents during an output current reference step change at $t = 0$. The energy errors of the same experiment are shown with blue and red traces in Fig. 12.

optimized gains are used in comparison to the gray traces which correspond to the traditional setting (see Table II). Additionally, the normalized sum of the squared errors

$$K_n = \frac{K}{K|_{t=0}} \tag{42}$$

$$K = e^2_{d0,\mathrm{err}} + \underline{e}_{s,\mathrm{err}}\underline{e}^*_{s,\mathrm{err}} + \underline{e}_{d,\mathrm{err}}\underline{e}^*_{d,\mathrm{err}} \tag{43}$$

is shown in Fig. 8(d), which falls below 10 % of its initial value already after 19 ms for the optimized setting. This means a 50% improvement over the traditional settings, which take as long as 39 ms for the same decay. In view of this improvement, the initially slower reduction of the errors is insignificant.

The higher gains of the optimized settings demand a moderate increase of the circulating current, as visible in Fig. 8(e), which can easily be accepted in view of the much faster decay.

The simulations in Fig. 8 assume zero common-mode voltage in compliance with the requirement $v_{y0} = 0$, which eases the solution of (23) and enables the eigenvalue optimization in the first place. This is only a minor drawback of the methodology, because the common-mode voltage is small compared to the output voltage in the normal operation region with high modulation index around the nominal frequency. A similar performance can be expected from the optimized settings when applied in an operation regime that uses the common-mode voltage to extend the linear modulation range. This is demonstrated in Fig. 9 in which the optimized settings are used for an operation that relies on a triplen harmonic injection of the common-mode voltage. Only moderate alterations are visible in the decay of the energy errors when the initial angle θ_0 is varied, which confirms the assumption that the optimized settings are suitable for this type of operation as well.

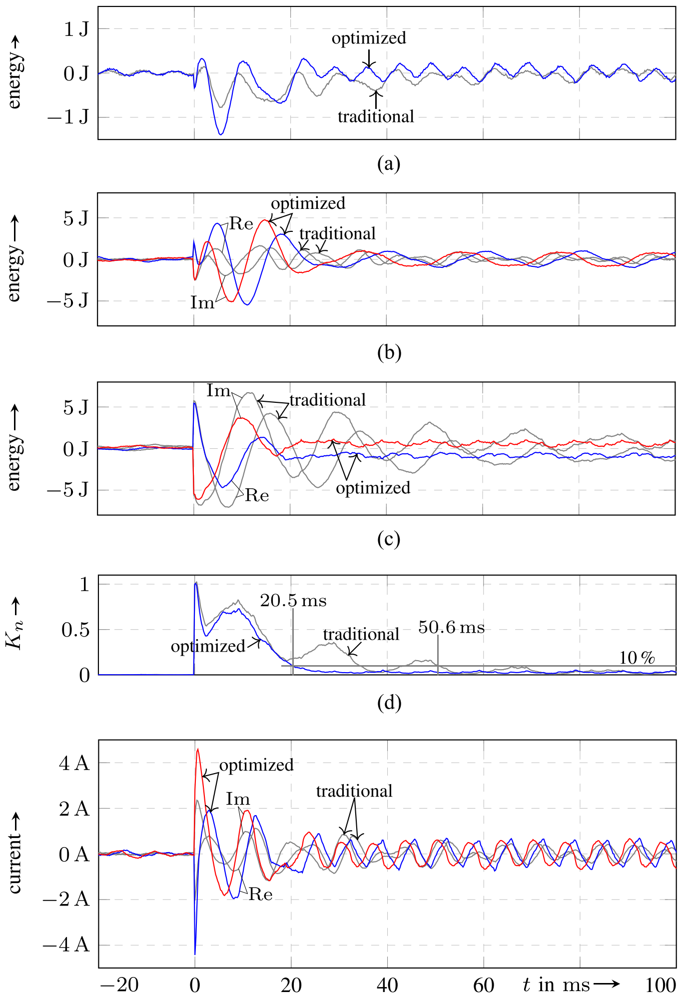

(a)

(b)

(c)

(d)

(e)

Fig. 12. Experimental comparison of the optimized settings (blue and red) with the traditional gains (gray), see Table II: (a) Error $e_{d0,\mathrm{err}}$ of the vertical difference; (b) Error $\underline{e}_{s,\mathrm{err}}$ of the complex sum; (c) Error $\underline{e}_{d,\mathrm{err}}$ of the complex difference; (d) Normalized sum of the squared errors (43); (e) Balancing circulating current $\underline{i}_{s,b}$ according to (18b). measurement results of the energy errors (a)–(c) and the balancing circulating current (e). The corresponding measurements of the ac current and the arm variables are shown in Figs. 10 and 11.

V. EXPERIMENTAL VERIFICATION

The gain settings are verified on a test bench by operating a grid-side MMC in rectifier mode and feeding a constant voltage electronic load on the dc side. Figs. 10 and 11 show the cell voltages, duty-cycles, two arm currents, and the grid currents

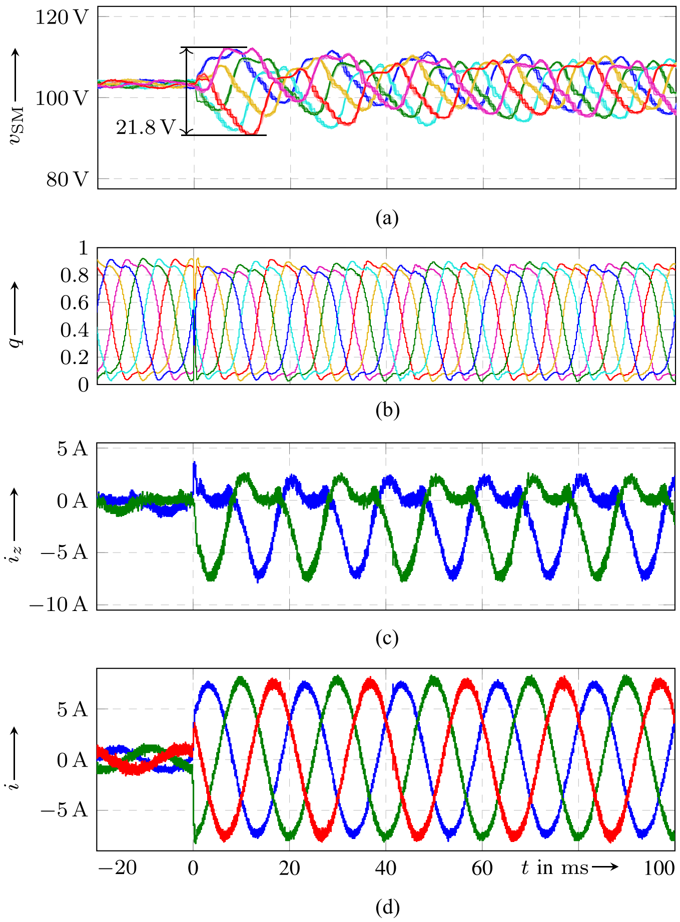

Fig. 13. Measurement results of the traditional gain settings (Table II) when a second harmonic is used in the circulating current: (a) cell voltages, (b) duty-cycles, (c) arm currents, and (d) output currents during an output current reference step change at $t = 0$. The corresponding energy errors are shown in Fig. 15.

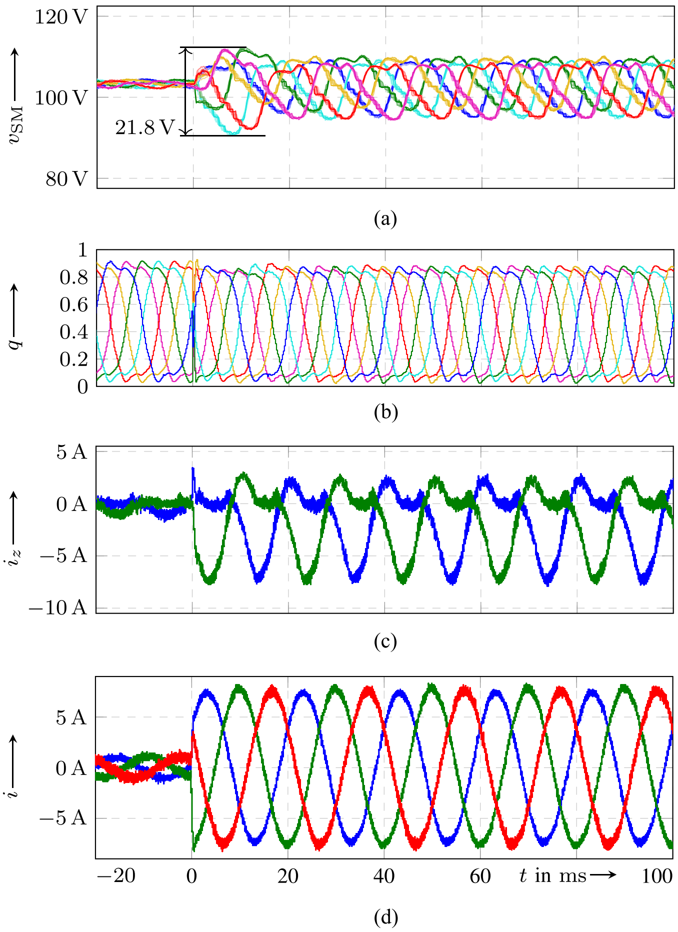

Fig. 14. Measurement results of the optimized gain settings (Table II) when a second harmonic is used in the circulating current: (a) cell voltages, (b) duty-cycles, (c) arm currents, and (d) output currents during an output current reference step change at $t = 0$. The corresponding energy errors are shown in Fig. 15.

for the traditional and the optimized settings from Table II, respectively. In contrast to the simulations, a base load of 1 A is provided to satisfy the minimum load requirements of the electronic load. The current reference changes to $\underline{I}$ at $t = 0$ and in a reaction to this, the balancing feedback adapts the energy distribution to the new stationary regime. The optimized setting much faster restores the cell voltages and even reduces their spread from 36.4 to 33.6 V, as evident from the traces in Figs. 10(a) and 11(a). The measurements in Fig. 10 and the simulation in Fig. 3 match reasonably well, although the cell voltage deviation is smaller in the simulation. Fig. 12 compares the energy errors of the same measurements.

The blue and red traces indicate the optimized setting and are taken from the same experiment as Fig. 11, while the traditional settings are indicated by gray lines and belong to the experiment in Fig. 10. Although the energy errors are reduced much quicker than with the traditional settings, small steady state errors remain in the energies which lead to a sustaining circulating current. The main reason is a considerable negative sequence ($> 2\%$) in the grid voltages, which disagrees to the assumed conditions for the energy reference determination. The traditional setting has an advantage in this regard, as its circulating current demand is lower during operation near the balanced regime. The measurement results of the decay times in Fig. 12(d) are slightly higher than the simulation results in Fig. 8(d) due to the disturbances neglected in the simulation. With the optimized settings, the 10%-threshold is reached after 20.5 ms while the traditional settings achieve the same decay after 50.5 ms, which corresponds to a performance improvement of more than 50% for the optimized gains.

Figs. 13 and 14 show measurement results for the traditional settings and the optimized gains, respectively, when a second harmonic is applied to the nominal circulating current to reduce the cell voltage ripple. The corresponding energy errors and the balancing circulating currents are given in Fig. 15. The gain settings are the same as in the former experiments, because the tuning process is identical since the error dynamics is valid for any nominal circulating current injection. In contrast to Figs. 10–12, the balancing demand after the step change is much lower due to the reduced voltage ripple, rendering this case uncritical. Even though no difference in the cell voltage spread can be observed [compare Figs. 13(a) and 14(a)], the control reserve on the upper duty cycle limit is slightly better for the optimized gains [compare Figs. 13(b) and 14(b)]. The normalized sum of

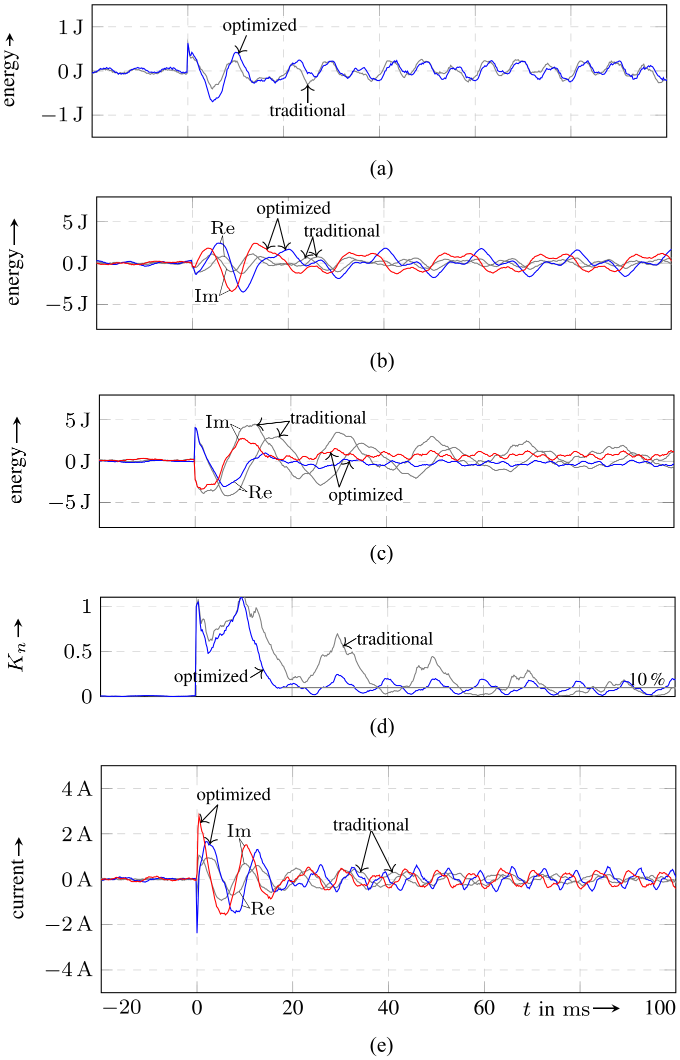

Fig. 15. Experimental comparison of the optimized settings (blue and red) with the traditional gains (gray) (see Table II) when a second harmonic is used in the circulating current: (a) Error $e_{d0,\mathrm{err}}$ of the vertical difference; (b) Error $\underline{e}_{s,\mathrm{err}}$ of the complex sum; (c) Error $\underline{e}_{d,\mathrm{err}}$ of the complex difference; (d) Normalized sum of the squared errors (43); (e) Balancing circulating current $\underline{i}_{s,b}$ according to (18b). The corresponding measurements of the ac current and the arm variables are shown in Figs. 13 and 14.

the squared errors in Fig. 15(d) will not fall below the 10% due to the small energy errors after the step change. Still, the stationary regime is reached earlier with the optimized gains as can be seen in Fig. 15(c). The measurements in Figs. 13–15 demonstrate the validity of the tuning process in presence of a nonzero nominal circulating current.

VI. CONCLUSION

A tuning methodology for the parameters of an MMC energy-balancing controller was proposed. In contrast to the traditional gain estimation on the open loop, an optimized set of gains was retrieved by eigenvalue analysis. The optimization was carried out after two preparative steps: in a first step, the error dynamics was extracted and the resulting model of the energy deviations from the desired balanced regime was successfully validated against a switched model of a complete MMC. In a second step, the error dynamics was transformed into a linear time invariant system by application of the theorem in [52] which gives convenient access to the eigenvalues. The optimization was targeted on eigenvalue constellations with equal (negative) real parts of the eigenvalues, as there were insufficient gains for a direct placement. The optimized gains were compared to the traditional settings which were estimated from an open-loop low-pass model of the energies. A simulation of the error dynamics demonstrates a superior performance of the optimized gains over the traditional settings. Although the eigenvalue calculation assumed zero common-mode voltage to ease the application of [52], similar performance can be expected from the optimized settings when used for an operation regime that relies on a common-mode voltage injection to extend the linear modulation range. This expectation was backed up by simulations of the error dynamics with common-mode voltage injection.

The proposed error dynamics extraction and eigenvalue optimization clearly outperforms the traditional estimation of the gains on an open-loop low-pass model, as demonstrated by simulations and measurements. The measurements on a low-voltage MMC in rectifier mode demonstrate a more than 50% reduction of the decay time and $> 7\%$ reduction of the dynamic cell voltage spread for the optimized settings. Additional experiments for the case of a second harmonic injection in the nominal circulating current reveal a faster decay of the energy errors for the optimized gains, adding more evidence to the wide applicability of the tuning method based on the simplified error dynamics.

Due to the convenient determination of balancing feedback eigenvalues, the proposed methodology opens up a multitude of different optimizations and tuning, by offering an unrestricted cost function design to the engineer. The slightly higher calculation effort is easily accepted in view of the superior performance.

APPENDIX

The appendix briefly recalls the tuning algorithm proposed in [32], [48]. The circulating current reference (18b) uses dedicated current components to solve the balancing problem. The mutual coupling that results from the common use of the circulating current entails a time delay until a balancing effect can be observed. In order to model this delay when the coupling is neglected, for each energy the low-pass model $G_o(s) = \frac{V_o}{s(1+sT_o)}$ is used which enables a simplified gain estimation. It consists of an integrator and a first-order delay. The gain V_o and the time constant T_o are chosen to reflect the individual behavior of each energy in order to estimate the (maximum) corresponding controller gain via $k = \frac{1}{2V_oT_o}$. For this purpose, the gain V_o and the time constant T_o can be identified. Table III summarizes this scheme taking the values from Table I as example.

In particular, the energies e_{d0} and $\underline{e}_d$ are expected to react slowly, because the desired power components have their origin in the ac powers $\mathrm{Re}(\underline{i}_s)\,\hat{v}_{y\Delta}$ and $\underline{a}_\theta^{-3}\underline{i}_s^*\hat{v}_{y\Delta}$, visible in (11b) and (11d), respectively. Following this reasoning, the delay is dominated by the output frequency ω, resulting in a corresponding time constant of $\frac{\pi}{2\omega}$, i.e. half of the ac period. By contrast, the energy $\underline{e}_s$ is expected to react faster, because the desired power component is generated with respect to the dc voltage v_{DC}, as

TABLE III
SIMPLIFIED GAIN ESTIMATION OF THE BALANCING FEEDBACK (18b) ACCORDING TO [32], [48]

gain in balancing feedback (18b)	k_0	k_s	k_d
respective energy	e_{d0}	$\underline{e}_s$	$\underline{e}_d$
open loop gain V_o	$\hat{v}_{y\Delta}$	v_{DC}	$\hat{v}_{y\Delta}$
time constant T_o	$\frac{\pi}{2\omega}$	$10T$	$\frac{\pi}{2\omega}$
values corresponding to Tab. I	$0.18\,\mathrm{A/J}$	$0.42\,\mathrm{A/J}$	$0.18\,\mathrm{A/J}$

seen in (11c). Thus, the dominating delay is set to ten sampling periods of the circulating current controller.

The gains for both, the vertical difference e_{d0} and the complex difference $\underline{e}_d$, depend on the output voltage because the desired power components in their respective subsystems are generated w.r.t $\hat{v}_{y\Delta}$. The gain for the complex energy sum $\underline{e}_s$ is given by the dc voltage v_{DC}.

This approach has been proposed in [32], [48], using a stationary frame, and, despite its drastic simplifications, gives a first clue about the permissible gain ranges.

REFERENCES

[1] M. Glinka and R. Marquardt, “A new AC/AC multilevel converter family,” *IEEE Trans. Ind. Electron.*, vol. 52, no. 3, pp. 662–669, Jun. 2005.

[2] C. Oates, “A methodology for developing ‘Chainlink’ converters,” in *Proc. Eur. Conf. Power Electron. Appl.*, Barcelona, Spain, Sep. 2009.

[3] H. Akagi, “Classification, terminology, and application of the modular multilevel cascade converter (MMCC),” *IEEE Trans. Power Electron.*, vol. 26, no. 11, pp. 3119–3130, Nov. 2011.

[4] L. Baruschka and A. Mertens, “A new three-phase AC/AC modular multilevel converter with six branches in hexagonal configuration,” *IEEE Trans. Ind. Appl.*, vol. 49, no. 3, pp. 1400–1410, May 2013.

[5] A. Mayer, C. Rolff, and R. Marquardt, “Control concept and stability considerations of the modular high frequency converter,” in *Proc. Eur. Conf. Power Electron. Appl.–Energy Convers. Cong. Expo. Eur.*, Lappeenranta, Finland, Aug. 2014.

[6] R. Marquardt, “Modular multilevel converter - Impact on future applications and semiconductors,” in *Proc. Power Electron. Compon. Their Appl.; 7. ETG-Symp.*, Apr. 2017.

[7] L. Huang *et al.*, “The evolution and variation of sub-module topologies with DC-fault current clearing capability in MMC-HVDC,” in *Proc. IEEE 3rd Int. Future Energy Electron. Conf. and Energy Convers. Cong. Expo. Asia*, Kaohsiung, Taiwan, Jun. 2017, pp. 1938–1943.

[8] A. Lesnicar and R. Marquardt, “An innovative modular multilevel converter topology suitable for a wide power range,” in *Proc. Power Tech Conf. Proc.*, Bologna, Italy, 2003, vol. 3.

[9] L. M. Cunico, G. Lambert, R. P. Dacol, S. V. G. Oliveira, and Y. R. de Novaes, “Parameters design for modular multilevel converter (MMC),” in *Proc. Brazilian Power Electron. Conf.*, Gramado, Brazil, Oct. 2013, pp. 264–270.

[10] C. Oates, “Modular multilevel converter design for VSC HVDC applications,” *IEEE J. Emerg. Sel. Topics Power Electron.*, vol. 3, no. 2, pp. 505–515, Jun. 2015.

[11] J. V. M. Farias, A. F. Cupertino, H. A. Pereira, S. I. S. Junior, and R. Teodorescu, “On the redundancy strategies of modular multilevel converters,” *IEEE Trans. Power Del.*, vol. 33, no. 2, pp. 851–860, Apr. 2018.

[12] B. Li, Y. Zhang, R. Yang, R. Xu, D. Xu, and W. Wang, “Seamless transition control for modular multilevel converters when inserting a cold-reserve redundant submodule,” *IEEE Trans. Power Electron.*, vol. 30, no. 8, pp. 4052–4057, Aug. 2015.

[13] K. Ilves, S. Norrga, L. Harnefors, and H.-P. Nee, “On energy storage requirements in modular multilevel converters,” *IEEE Trans. Power Electron.*, vol. 29, no. 1, pp. 77–88, 2014.

[14] H. Bärnklau, A. Gensior, and S. Bernet, “Submodule capacitor dimensioning for modular multilevel converters,” *IEEE Trans. Ind. Appl.*, vol. 50, no. 3, pp. 1915–1923, May 2014.

[15] M. Hiller, D. Krug, R. Sommer, and S. Rohner, “A new highly modular medium voltage converter topology for industrial drive applications,” in *Proc. Eur. Conf. Power Electron. Appl.*, Barcelona, Spain, Sep. 2009.

[16] S. Rohner, J. Weber, and S. Bernet, “Continuous model of modular multilevel converter with experimental verification,” in *Proc. IEEE Energy Convers. Cong. Expo.*, Phoenix, AZ, Sep. 2011, pp. 4021–4028.

[17] R. Marquardt, “Modular multilevel converter: An universal concept for HVDC-Networks and extended DC-Bus-applications,” in *Proc. Int. Power Electron. Conf.*, Sapporo, Japan, Jun. 2010, pp. 502–507.

[18] A. Dekka, B. Wu, R. L. Fuentes, M. A. Pérez, and N. R. Zargari, “Evolution of topologies, modeling, control schemes, and applications of modular multilevel converters,” *IEEE J. Emerg. Sel. Topics Power Electron.*, vol. 5, no. 4, pp. 1631–1656, Dec. 2017.

[19] R. Marquardt, A. Lesnicar, and J. Hildinger, “Modulares stromrichterkonzept für netzkupplungsanwendungen bei hohen spannungen,” in *Proc. ETG-Fachtagung*, Bad Nauheim, Germany, Apr. 2002.

[20] A. Lesnicar and R. Marquardt, “A new modular voltage source inverter topology,” in *Proc. Eur. Conf. Power Electron. Appl.*, Toulouse, France, Sep. 2003.

[21] J. Kolb, F. Kammerer, and M. Braun, “A novel control scheme for low frequency operation of the modular multilevel converter,” in *Proc. Power Electron., Intell. Motion Power Quality Eur.*, Nuremberg, Germany, May 2011, pp. 961–966.

[22] M. Schröder, S. Henninger, J. Jäger, A. Rašić, H. Rubenbauer, and T. Lang, “An enhanced modulator concept for the modular multilevel converter,” in *Proc. Eur. Conf. Power Electron. Appl.–Energy Convers. Cong. Expo. Eur.*, Lappeenranta, Finland, Aug. 2014.

[23] S. Fuchs, S. Beck, and J. Biela, “High output voltage precision PWM for modular multilevel converters,” in *Proc. Eur. Conf. Power Electron. Appl.–Energy Convers. Cong. Expo. Eur.*, Warsaw, Poland, Sep. 2017.

[24] D. Siemaszko, “Fast sorting method for balancing capacitor voltages in modular multilevel converters,” *IEEE Trans. Power Electron.*, vol. 30, no. 1, pp. 463–470, Jan. 2015.

[25] V. Hofmann and M.-M. Bakran, “A capacitor voltage balancing algorithm for hybrid modular multilevel converters in HVDC applications,” in *Proc. PEDS*, Honolulu, HI, Dec. 2017, pp. 691–696.

[26] A. Pérez-Basante, S. Ceballos, G. Konstantinou, M. Liserre, J. Pou, and I. M. de Alegría, “Circulating current control for modular multilevel converter based on selective harmonic elimination with ultra-low switching frequency,” in *Proc. Eur. Conf. Power Electron. Appl.–Energy Convers. Cong. Expo. Eur.*, Karlsruhe, Germany, Sep. 2016.

[27] F. Hahn, M. Andresen, G. Buticchi, and M. Liserre, “Thermal analysis and balancing for modular multilevel converters in HVDC applications,” *IEEE Trans. Power Electron.*, vol. 33, no. 3, pp. 1985–1996, Mar. 2018.

[28] L. Ängquist, A. Antonopoulos, D. Siemaszko, K. Ilves, M. Vasiladiotis, and H.-P. Nee, “Inner control of modular multilevel converters - an approach using open-loop estimation of stored energy,” in *Proc. Int. Power Electron. Conf.*, Sapporo, Japan, Jun. 2010, pp. 1579–1585.

[29] A. J. Korn, M. Winkelnkemper, and P. Steimer, “Low output frequency operation of the modular multi-level converter,” in *Proc. Energy Convers. Cong. Expo. Eur.*, Atlanta, GA, Sep. 2010, pp. 3993–3997.

[30] P. Münch, D. Görges, M. Izák, and S. Liu, “Integrated current control, energy control and energy balancing of modular multilevel converters,” in *Proc. IECON*, Glendale, AZ, 2010, pp. 150–155.

[31] S. P. Engel and R. W. De Doncker, “Control of the modular multi-level converter for minimized cell capacitance,” in *Proc. Eur. Conf. Power Electron. Appl.*, Birmingham, UK, Aug. 2011.

[32] J. Kolb, F. Kammerer, M. Gommeringer, and M. Braun, “Cascaded control system of the modular multilevel converter for feeding variable-speed drives,” *IEEE Trans. Power Electron.*, vol. 30, no. 1, pp. 349–357, Jan. 2015.

[33] H. R. Parikh, R. S. M. Loeches, G. Tsolaridis, R. Teodorescu, L. Mathe, and S. Chaudhary, “Capacitor voltage ripple reduction and arm energy balancing in MMC-HVDC,” in *Proc. IEEE 16th Int. Conf. Environ. Electr. Eng.*, Florence, Italy, Jun. 2016.

[34] Y. Okazaki, H. Matsui, M. M. Muhoro, M. Hagiwara, and H. Akagi, “Capacitor-voltage balancing for a modular multilevel DSCC inverter driving a medium-voltage synchronous motor,” *IEEE Trans. Ind. Appl.*, vol. 52, no. 5, pp. 4074–4083, Sep. 2016.

[35] F. Deng and Z. Chen, “Voltage-balancing method for modular multilevel converters under phase-shifted carrier-based pulsewidth modulation,” *IEEE Trans. Ind. Electron.*, vol. 62, no. 7, pp. 4158–4169, Jul. 2015.

[36] A. E. Leon and S. J. Amodeo, "Energy balancing improvement of modular multilevel converters under unbalanced grid conditions," *IEEE Trans. Power Electron.*, vol. 32, no. 8, pp. 6628–6637, Aug. 2017.

[37] Y. Wang and R. Marquardt, "Novel control scheme for the internal energies and circulating currents of modular multilevel converter," in *Proc. Power Electron., Intell. Motion Power Quality Eur. Eur.*, Nuremberg, Germany, May 2017.

[38] M. Lu, J. Hu, R. Zeng, and Z. He, "Fundamental-frequency reactive circulating current injection for capacitor voltage balancing in hybrid-MMC HVDC systems during riding through PTG faults," *IEEE Trans. Power Del.*, vol. 33, no. 3, pp. 1348–1357, Jun. 2018.

[39] S. Cui and S.-K. Sul, "A comprehensive DC short-circuit fault ride through strategy of hybrid modular multilevel converters (MMCs) for overhead line transmission," *IEEE Trans. Power Electron.*, vol. 31, no. 11, pp. 7780–7796, Nov. 2016.

[40] G. Bergna, M. Pirro, E. Berne, A. Arzandé, M. M. Cabrera, and R. Ortega, "Modular multilevel converter passivity-based PI control suited for balanced and unbalanced grid conditions," in *Proc. IEEE Int. Conf. Ind. Technol.*, Mar. 2015, pp. 3072–3078.

[41] S. Debnath, J. Qin, B. Bahrani, M. Saeedifard, and P. Barbosa, "Operation, control, and applications of the modular multilevel converter: A review," *IEEE Trans. Power Electron.*, vol. 30, no. 1, pp. 37–53, Jan. 2015.

[42] M. Schröder, F. Mahr, J. Jäger, and S. Hänsel, "Energy balancing in the modular multilevel converter under unbalanced grid conditions," in *Proc. Eur. Conf. Power Electron. Appl.–Energy Convers. Cong. Expo. Eur.*, Warsaw, Poland, Sep. 2017.

[43] M. Jankovic, A. Costabeber, A. Watson, and J. C. Clare, "Arm-balancing control and experimental validation of a grid-connected MMC with pulsed DC load," *IEEE Trans. Ind. Electron.*, vol. 64, no. 12, pp. 9180–9190, Dec. 2017.

[44] T. Soong and P. W. Lehn, "Internal power flow of a modular multilevel converter with distributed energy resources," *IEEE J. Emerg. Sel. Topics Power Electron.*, vol. 2, no. 4, pp. 1127–1138, Dec. 2014.

[45] G. Henke and M.-M. Bakran, "Balancing of modular multilevel converters with unbalanced integration of energy storage devices," in *Proc. Eur. Conf. Power Electron. Appl.–Energy Convers. Cong. Expo. Eur.*, Karlsruhe, Germany, Sep. 2016.

[46] P. Himmelmann and M. Hiller, "A generalized approach to the analysis and control of modular multilevel converters," in *Proc. Power Electron., Intell. Motion Power Quality Eur. Eur.*, Nuremberg, Germany, May 2017.

[47] D. Karwatzki and A. Mertens, "Generalized control approach for a class of modular multilevel converter topologies," *IEEE Trans. Power Electron.*, vol. 33, no. 4, pp. 2888–2900, Apr. 2018.

[48] J. Kolb, "Optimale Betriebsführung des Modularen Multilevel-Umrichters als Antriebsumrichter für Drehstrommaschinen," Ph.D. dissertation, Karlsruher Institut für Technologie, 2013.

[49] N. Stanković, G. Bergna, A. Arzandé, E. Berne, P. Egrot, and J.-C. Vannier, "An optimization-based control strategy for modular multilevel converters: Design and implementation," in *Proc. PEDS*, Sydney, Australia, Jun. 2015, pp. 12–17.

[50] G. Bergna *et al.*, "A generalized power control approach in ABC frame for modular multilevel converter HVDC links based on mathematical optimization," *IEEE Trans. Power Del.*, vol. 29, no. 1, pp. 386–394, Feb. 2014.

[51] D. Karwatzki, L. Baruschka, M. Dokus, J. Kucka, and A. Mertens, "Branch energy balancing with a generalised control concept for modular multilevel topologies – using the example of the modular multilevel converter," in *Proc. Eur. Conf. Power Electron. Appl.–Energy Convers. Cong. Expo. Eur.*, Karlsruhe, Germany, Sep. 2016.

[52] M.-Y. Wu, "Some new results in linear time-varying systems," *IEEE Trans. Autom. Control*, vol. 20, no. 1, pp. 159–161, Feb. 1975.

[53] H. Bärnklau, A. Gensior, and S. Bernet, "Derivation of an equivalent submodule per arm for modular multilevel converters," in *Proc. 15th Int. Power Electron. Motion Control Conf.–Energy Convers. Cong. Expo. Eur.*, Novi Sad, Serbia, 2012, pp. LS2a.2–1–LS2a.2–5.

[54] M. A. Pérez, S. Bernet, J. Rodríguez, S. Kouro, and R. Lizana, "Circuit topologies, modeling, control schemes, and applications of modular multilevel converters," *IEEE Trans. Power Electron.*, vol. 30, no. 1, pp. 4–17, Jan. 2015.

[55] H. Fehr and A. Gensior, "Improved energy balancing of grid side modular multilevel converters by optimized feed-forward circulating currents and common-mode voltage," *IEEE Trans. Power Electron.*, vol. 33, no. 12, pp. 10 903–10 913, Dec. 2018.

[56] H. Li *et al.*, "Hardware design of a 1.7 kV SiC MOSFET based MMC for medium voltage motor drives," in *Proc. IEEE Appl. Power Electron. Conf. Expo.*, Mar. 2018, pp. 1649–1655.

[57] J. Kucka, D. Karwatzki, L. Baruschka, and A. Mertens, "Improved modular multilevel converter topology with magnetically coupled branch inductors," in *Proc. Energy Convers. Cong. Expo.*, Montreal, Canada, Sep. 2015, pp. 3593–3600.

[58] M. Hagiwara, R. Maeda, and H. Akagi, "Negative-sequence reactive-power control by the modular multilevel cascade converter based on double-star chopper-cells (MMCC-DSCC)," in *Proc. Energy Convers. Cong. Expo.*, Atlanta, GA, Sep. 2010, pp. 3949–3954.

[59] X. Shi, Z. Wang, L. M. Tolbert, and F. Wang, "Modular multilevel converters with integrated arm inductors for high quality current waveforms," in *Proc. IEEE Energy Convers. Cong. Expo. Asia Downunder*, Jun. 2013, pp. 636–642.

[60] M. Espinoza-B. *et al.*, "An integrated converter and machine control system for MMC-based high power drives," *IEEE Trans. Ind. Electron.*, vol. 66, no. 3, pp. 2343–2354, Mar. 2019.

[61] J. Pou, S. Ceballos, G. Konstantinou, V. G. Agelidis, R. Picas, and J. Zaragoza, "Circulating current injection methods based on instantaneous information for the modular multilevel converter," *IEEE Trans. Ind. Electron.*, vol. 62, no. 2, pp. 777–788, Feb. 2015.

[62] J. Hu, L. Lin, M. Xiang, M. Lu, J. Zhu, and Z. He, "Improved design and control of FBSM MMC with boosted AC voltage and reduced DC capacitance," *IEEE Trans. Ind. Electron.*, vol. 65, no. 3, pp. 1919–1930, Mar. 2018.

[63] A. Dudin, A. Fidelak, and J. Petzoldt, "Effect of the loss-minimizing circulating current on the modular multilevel converter with IGBT switches," in *Proc. Eur. Conf. Power Electron. Appl.–Energy Convers. Cong. Expo. Eur.*, Karlsruhe, Germany, Sep. 2016.

[64] M. Middeke, H. Fehr, and A. Gensior, "Reducing the modulation voltage error in MMCs by considering the capacitor voltage change within one PWM cycle for improved current control," in *Proc. Eur. Conf. Power Electron. Appl.–Energy Convers. Cong. Expo. Eur.*, Warsaw, Poland, Sep. 2017.

[65] S. Fuchs, S. Beck, and J. Biela, "Analysis and reduction of the output voltage error of PWM for modular multilevel converters," *IEEE Trans. Ind. Electron.*, vol. 66, no. 3, pp. 2291–2301, Mar. 2019.

[66] A. M. Lopez, D. E. Quevedo, R. P. Aguilera, T. Geyer, and N. Oikonomou, "Limitations and accuracy of a continuous reduced-order model for modular multilevel converters," *IEEE Trans. Power Electron.*, vol. 33, no. 7, pp. 6292–6303, Jul. 2018.

[67] D. Schröder, *Elektrische Antriebe – Regelung von Antriebssystemen*, 3rd ed. Springer-Verlag, Berlin Heidelberg, 2009.

Hendrik Fehr received the Dipl.-Ing. degree in Elektrotechnik from the Technische Universität Dresden, (TU Dresden), Dresden, Germany, in 2008.

He is currently with the Professur Leistungselektronik, Elektrotechnisches Institut, TU Dresden.

His research interests include modulation and control of power electronic converters, sliding mode, and flatness-based methods.

Albrecht Gensior received the Dipl.-Ing. and Dr.-Ing. degrees in Elektrotechnik from the Technische Universität Dresden, (TU Dresden), Dresden, Germany, in 2003 and 2008, respectively.

He is currently with the Professur Leistungselektronik, Elektrotechnisches Institut, TU Dresden, where he is involved in research projects dealing with the control of power electronic converters and drives.

His research interest is mainly in nonlinear controller design and observers for these applications.